



Review

Recent Progress in Halide Perovskite Nanocrystals for Photocatalytic Hydrogen Evolution

Zhijie Zhang ^{*}, Rui Zhou, Deben Li, Ying Jiang, Xuesheng Wang, Huiling Tang and Jiayue Xu ^{*}

School of Materials Science and Engineering, Shanghai Institute of Technology, 100 Haiquan Road, Shanghai 201418, China

^{*} Correspondence: zjzhang@sit.edu.cn (Z.Z.); xujiayue@sit.edu.cn (J.X.)

Abstract: Due to its environmental cleanliness and high energy density, hydrogen has been deemed as a promising alternative to traditional fossil fuels. Photocatalytic water-splitting using semiconductor materials is a good prospect for hydrogen production in terms of renewable solar energy utilization. In recent years, halide perovskite nanocrystals (NCs) are emerging as a new class of fascinating nanomaterial for light harvesting and photocatalytic applications. This is due to their appealing optoelectronic properties, such as optimal band gaps, high absorption coefficient, high carrier mobility, long carrier diffusion length, etc. In this review, recent progress in halide perovskite NCs for photocatalytic hydrogen evolution is summarized. Emphasis is given to the current strategies that enhance the photocatalytic hydrogen production performance of halide perovskite NCs. Some scientific challenges and perspectives for halide perovskite photocatalysts are also proposed and discussed. It is anticipated that this review will provide valuable references for the future development of halide perovskite-based photocatalysts used in highly efficient hydrogen evolution.

Keywords: halide perovskite nanocrystals; photocatalysis; hydrogen evolution; heterojunction; charge separation



Citation: Zhang, Z.; Zhou, R.; Li, D.; Jiang, Y.; Wang, X.; Tang, H.; Xu, J. Recent Progress in Halide Perovskite Nanocrystals for Photocatalytic Hydrogen Evolution. *Nanomaterials* **2023**, *13*, 106. <https://doi.org/10.3390/nano13010106>

Academic Editor: Chiara Maccato

Received: 28 November 2022

Revised: 19 December 2022

Accepted: 23 December 2022

Published: 25 December 2022



Copyright: © 2022 by the authors. Licensee MDPI, Basel, Switzerland. This article is an open access article distributed under the terms and conditions of the Creative Commons Attribution (CC BY) license (<https://creativecommons.org/licenses/by/4.0/>).

1. Introduction

With the rapid growth of human consumption, the world is faced with surging energy demands amidst the quick depletion of fossil fuels and severe natural environmental issues. To alleviate the threat of energy crisis and environmental deterioration, it is urgent to seek more eco-friendly and sustainable renewable energy sources. As a carbon-free and clean energy source, hydrogen has been deemed as a promising future energy source to replace traditional fossil fuels [1–3]. Among various approaches to hydrogen generation, photocatalytic water splitting utilizing abundant solar energy and semiconductor materials has been regarded as one of the most attractive routes. In the photocatalysis field, the rational design and fabrication of advanced photocatalysts with ideal solar-to-hydrogen (STH) energy conversion efficiency is the most critical aspect [4,5]. Since the pioneering work of photoelectrochemical water splitting on TiO₂ electrodes by Fujishima and Honda [6], the field of hydrogen production from water splitting has been systematically investigated, which includes exploring the basic photocatalytic mechanism, developing novel photocatalytic materials, and designing efficient photocatalytic systems. Generally, the fundamental working principle of photocatalysis includes the absorption of light energy by semiconductors to create electron-hole pairs, which then migrate to the semiconductor's surface to initiate redox reactions. Thus, the separated electron-hole pairs play crucial roles in the photocatalytic redox reaction. To date, various kinds of semiconductor photocatalysts have been developed for hydrogen generation, including oxides (CeO₂, WO₃, Ga₂O₃, etc.) [7–17], sulfides (CdS, MoS₂, ZnS, etc.) [18–27], C₃N₄ [28–33], etc. However, conventional semiconductor photocatalysts still have a low STH energy conversion efficiency that is far from satisfactory due to their wide bandgaps and high electron-hole recombination rates.

Recently, halide perovskite materials—on account of their fascinating electronic and optical properties, including outstanding visible light harvesting ability, suitable band positions to provide sufficient driving potential, as well as their high carrier mobility and long electron-hole diffusion lengths—have emerged as a class of promising candidates for photocatalytic applications. To date, various kinds of halide perovskites, in either an organic–inorganic or all-inorganic fashion (e.g., $\text{CH}_3\text{NH}_3\text{PbX}_3$, CsPbX_3 , $X = \text{Cl}, \text{Br}, \text{I}$), have shown great potential in photocatalysis fields such as CO_2 reduction [34–40], hydrogen generation [41–45], pollutant degradation [46–51], phenethylol oxidation [52,53], organic reaction [54,55], etc. Since the first demonstration of using methylammonium lead iodide ($\text{CH}_3\text{NH}_3\text{PbI}_3$, MAPbI_3) for hydrogen generation via the solar-driven splitting of hydrogen iodide by Park et al. [44], the potential of halide perovskites for photocatalytic hydrogen production has been investigated by many researchers. In virtue of the advantages of halide perovskites mentioned above, such as the excellent light-absorption ability and suitable band positions, the applications of these materials in photocatalytic hydrogen production begin to flourish and exhibit outstanding photocatalytic performances.

In this review, we summarize the recent progress made in using halide perovskites for solar-driven photocatalytic hydrogen production. To date, numerous review articles have summarized recent advances in halide perovskites applied in solar energy conversion. In contrast to previous reviews, this review focuses exclusively on the application of halide perovskites in photocatalytic hydrogen production. Firstly, we introduced the property and photocatalytic mechanism of halide perovskites, and highlighted strategies used for enhancing the photocatalytic hydrogen production performance of these materials. Finally, we concluded by introducing a perspective on the future challenges and opportunities of this field, which could provide guidelines for further research on halide perovskite-based photocatalysis applications.

2. Properties of Halide Perovskites

2.1. The Composition of Halide Perovskites

Halide perovskite materials have a general structural formula of ABX_3 (Figure 1a), where A is usually a monovalent cation (Cs^+ , methylammonium (MA^+), or formamidinium (FA^+)), B is a divalent metal ion (Pb^{2+} , Sn^{2+} , or Ge^{2+}), and X is the halogen anion, namely I^- , Br^- , or Cl^- [56,57]. The B cation coordinates with six halogen anions to form $[\text{BX}_6]^{4-}$ octahedra. The large monovalent A cation behaves like a total charge neutralizer, which is bridged to a network of corner-sharing BX_6 octahedrons, forming the ideal perovskite structure. The A-, B-, and C-site ions can be substituted isomorphically by other similar ions, thus altering the defect properties, electronic structure, and catalytic performance of the material [58–61]. Both the B and X ions play an important part in governing the band structure of halide perovskites that affects their catalytic performance, while the function of the A cation is ignorable. Although the A cation generally does not construct the energy level, its size plays a crucial role in judging the formability of the perovskite structure, since either a smaller or larger A cation could lead to either a contraction or expansion of the perovskite lattice. Usually, perovskites exhibit a cubic structure (space group: $\text{Pm}\bar{3}\text{m}$), which can transform into orthorhombic (space group: Pnma) or tetragonal (space group: I4/mcm) phase when the temperature decreases [62–64]. As observed in the crystal structure, the B-site cation and the anion are tightly bound, while the A-site cation and the anion have a weak interaction. The BX_6 octahedral structure can be distorted by the difference between the electronegativities and ionic radii of the A and B cations, leading to a weakened symmetry of the crystal structure. It has been proved that the tilt angle can affect the electronic band structure, photoluminescence, dielectric, and the charge transport properties of the perovskites [65–67]. Various types of perovskite crystals with desirable characteristics can be designed by adjusting these interactions via placing different types of cations at corresponding lattice sites [68,69].

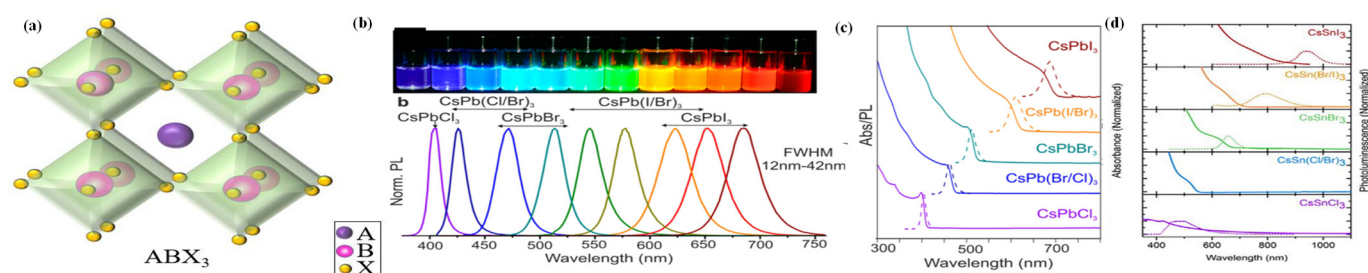


Figure 1. (a) Schematic illustration of the crystal structure of halide perovskite. (b) Colloidal halide perovskite CsPbX_3 NCs ($X = \text{Cl}, \text{Br},$ and I) exhibit size- and composition-tunable bandgap energies covering the entire visible spectral region with narrow and bright emission. (c) Typical optical absorption and PL spectra of CsPbX_3 NCs. (d) Typical optical absorption and PL spectra of CsSnX_3 NCs. (b,c) Reproduced with permission [70]. Copyright: 2015, American Chemical Society. (d) Reproduced with permission [71]. Copyright: 2016, American Chemical Society.

2.2. Optoelectronic Properties of Halide Perovskites

Understanding the composition, crystal structure, and the electronic band structure of the perovskite is of vital importance because these pivotal factors are intercorrelated in judging its potentiality for satisfactory photocatalytic performances. The energy band structure of halide perovskites consists of an antibonding valence band maximum (VBM) and an antibonding conduction band minimum (CBM) system, rendering this crystal with high defect tolerance. Applying DFT calculations, the VBM of perovskites is composed of an antibonding hybrid state between the 6s orbital of B and the np orbital of X ($n = 3, 4,$ and 5 for $\text{Cl}, \text{Br},$ and I , respectively), with the np orbital of X as the major contributor, whereas the CBM is formed from an antibonding hybrid state between 6p orbitals of B and np orbitals of X, with 6p orbitals of B as the significant contributor [72,73]. Taking cubic CsPbBr_3 QDs as an example, its CB and VB positions are determined based on the 6p orbital of Pb and the 4p orbital of Br, respectively, whereas Cs has negligible effect on the energy band edge [74]. Since the A-site cations exhibit no significant effect on the VBM or CBM [75], the bandgap tuning can be easily realized by mixing or exchanging the halogen anions. For example, by altering the ratio of different halide ions, Sargent and his co-workers successfully tuned the bandgap of MAPbI_3 [76]. When the iodide concentration was increased, the absorption and emission spectra of the $\text{CsPbBr}_{3-x}\text{I}_x$ perovskite film red-shifted to longer wavelength, and its bandgap became narrower [77]. The tunable bandgap affords a good platform to modulate the energy band edge of halide perovskites toward highly efficient photocatalytic performance for various applications. For instance, Guo et al. reported that the band edge positions of $\text{CsPb}(\text{Br}_x/\text{Cl}_{1-x})_3$ could be tuned by regulating the ratio of Br and Cl [78], and the photocatalytic activity toward CO_2 reduction is significantly enhanced.

Generally, halide perovskites are considered as direct bandgap semiconductors. For MAPbI_3 , the spin-orbit coupling leads to Rashba splitting of the conduction band, resulting in a weak indirect bandgap of 60 meV during the direct bandgap transition [79]. Halide perovskites exhibit photo-absorption in almost the entire visible region, indicating that charge carriers can be effectively produced upon low energy excitation, which is favourable to photocatalytic applications [80,81]. A practical strategy to realize spectral absorption diversity and bandgap tuning with perovskites is adopting mixed halides. For example, by only altering the halogen element at the X-site from Cl to Br to I, Protesescu et al. found a redshift of the emission wavelength of CsPbX_3 ($X = \text{Cl}, \text{Br},$ or I) from 410 nm to 512 nm and 700 nm, and to any other intermediate wavelengths within the visible spectral range using mixed halide ions (Figure 1b,c) [70]. However, as the halogen composition changes, the valence band edge moves by a relatively wide margin within the energy levels, while the conduction band edge exhibits little change. For the MAPbX_3 perovskite, when X was Cl to I, the emission wavelength shifted from 403 to 740 nm [82].

In addition, the B-site cation also has a significant effect on the optical properties of halide perovskites. Inevitably, the Pb element in perovskites need to be partially or completely replaced due to environmental issues. Compared to those of CsPbX₃, strong red shifts of the absorption and emission spectra were observed for CsSnX₃, from 443 nm (X = Cl) to 953 nm (X = I) (Figure 1d) [71]. By compositional modulation, the bandgaps of halide perovskites can be designed and tuned within a certain range, achieving targeted energy levels. In addition, optical properties of halide perovskites can be enhanced by a metal ion doping strategy. For example, by doping Cu²⁺ and Sb³⁺ into the three octahedral layers, the layered double perovskite Cs₄CuSb₂Cl₁₂ was obtained. It has a direct band gap of 1.0 eV, and an electrical conductivity one order of magnitude higher than that of MAPbI₃ [83]. In addition, the partial replacement of Pb by Mn may cause a strong Stokes shift in the emission, which can increase the utilization rate of sunlight [84]. However, the incorporation of cations (Cd²⁺, Al²⁺, and Zn²⁺) into the halide perovskite can cause shrinkage of the original lattice, resulting in a wider bandgap, blueshift of the absorption peak, and weaker absorption ability [85–87].

3. Applications of Halide Perovskites in Photocatalytic Hydrogen Evolution

3.1. Basic Principle of Photocatalysis with Halide Perovskites

Photocatalytic redox reactions driven by semiconductor materials usually involve identically essential steps (Figure 2a) [88]: (1) generation of electron-hole pairs by the light harvesting of the photocatalyst, (2) transfer of photogenerated electrons and holes to the surface of the photocatalyst, and (3) photogenerated charge carriers participate in redox reactions. In order to drive the water-splitting redox reactions, the VB edge of the semiconductor should be more positive than the oxidation potential of H₂O to O₂ (1.23 V vs. normal hydrogen electrode [NHE], pH = 0), while the CB edge of the semiconductor should be more negative than the reduction potential of H⁺ to H₂ (0 V vs. NHE, pH = 0) [89]. So, theoretically, the minimum bandgap required for water splitting is 1.23 eV. However, considering the overpotential associated with the water-splitting redox reactions, the bandgap to drive efficient overall water splitting must be further widened, usually to 1.8–2.0 eV [90–92]. The relative positions of CB and VB potentials for most halide perovskites are shown in Figure 2b, along with the redox potentials of photocatalytic half-reactions associated with water splitting, CO₂ reduction, etc. Apparently, the CB potentials of most halide perovskites are more negative than the reduction potential of H⁺ to H₂, meeting the thermodynamic requirements for reducing water. In other words, the relative CB positions of halide perovskites are usually sufficient for H₂ production, exhibiting excellent reduction abilities. Theoretically, some members of halide perovskites (such as all-inorganic CsPbBr₃) can also oxidize water to produce O₂ because their VB potentials are relatively positive.

In addition, factors like the molar extinction coefficient, charge carrier recombination, and defect state of a halide perovskite should also be taken into account for photocatalytic applications [93–95]. A high molar extinction coefficient (ϵ) is essential for efficient absorption of visible light and generation of excitons [96]. The ϵ values of colloidal perovskites, ranging from about 10⁵ to 10⁷ L mol⁻¹ cm⁻¹, are comparable to those of a-Si: H and GaAs, and an order of magnitude higher than that of c-Si, which are representative photovoltaic materials [97,98]. This is indicative of better visible light responses for halide perovskites, thus improving photon-carrier conversion efficiencies [99]. However, the ϵ value of a halide perovskite is also dependent on the size of the crystals. This is especially important in the nanometer size range due to the quantification effect, which needs to be taken into account for practical applications in optoelectronics [100].

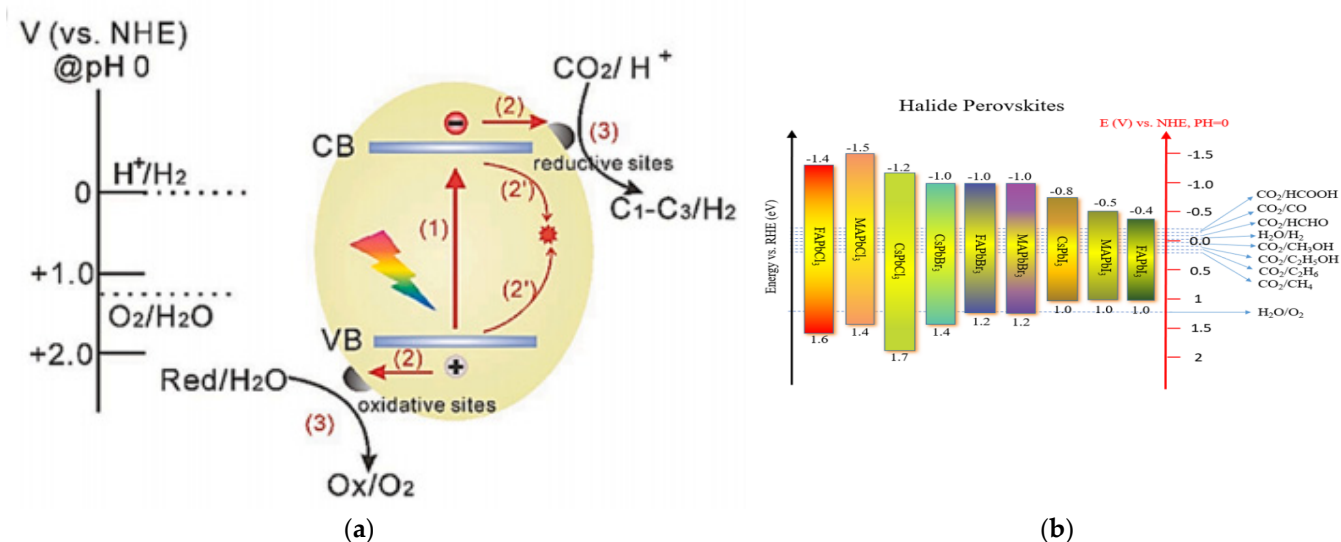


Figure 2. (a) Schematic illustration of charge transfer reactions that may occur at the surface and in the bulk of a semiconductor photocatalyst. (b) Energy levels of halide perovskites with the relative potential in photocatalytic applications. (a) Reproduced with permission [88]. Copyright: 2020, Wiley.

Carrier diffusion length is also important for the photocatalytic applications of halide perovskites. Generally, a longer carrier diffusion length indicates a lower recombination rate. The carrier diffusion lengths of halide perovskites have been increased by various strategies. For example, Dong et al. used a solution-growth method to obtain MAPbI₃ single crystals with a high carrier diffusion length exceeding 175 μm , which could be attributed to the long lifetime, high carrier mobility, and small trap densities of the single crystals [101], whereas the polycrystalline MAPbI₃ has a charge carrier diffusion of only ca. 100 nm. By incorporating Cl⁻ into MAPbI_{3-x}Cl_x, Zhang et al. obtained a perovskite with a carrier diffusion length of up to 380 μm [102]. This is because the incorporation of Cl⁻ can increase the density of trap states, thus creating the medium for carrier transfer and reducing the VB, which play a dominant role in charge recombination. As a consequence, maximum values of the carrier diffusion lengths were reached for the MAPbI_{3-x}Cl_x single crystals with the optimum Cl content ($x = 0.005$). Owing to the enhanced utilization of photogenerated charge carriers, it is expected that the long carrier diffusion length of halide perovskites would significantly contribute to their catalytic activity.

In addition, the photogenerated charge transfer kinetics in halide perovskites are also vital for the design of highly efficient photocatalysts. Excitons and free carriers are produced rapidly under light excitation, with free carriers as the main light-excited species. In most cases, excitons are also rapidly decomposed into free carriers. For instance, the excitons in CsPbBr₃ NCs are quickly converted into free carriers after 4–5 ps [103]. These hot carriers relax to the energy band edge via carrier-phonon and carrier-carrier interactions within fs. The larger the size of halide perovskite nanocrystals is, the faster the cooling kinetics of hot carriers is [104]. As the lifetime of a hot carrier in perovskites increases, the carrier becomes relatively easy to extract. Radiative recombination of cooled carriers takes place within ns at the band edge. For example, the capture time of non-radiative carriers in CsPbBr₃ NCs is about 40–50 ps [105]. On account of the defect tolerance features of halide perovskites, the energies of carriers in the defects are similar to those of edge carriers, which implies that more high-energy carriers will make potential contributions to photocatalytic reactions. For CsPbBr₃, the carriers can be extracted by electron-hole acceptors within ps, indicating that the extracted carriers can be potentially applied in photocatalysis [106]. Therefore, the ideal energy levels, along with the unique charge transfer kinetics, make halide perovskites good candidates for photocatalytic applications [107]. To sum up, halide perovskites provide distinct advantages for photocatalysis: (1) targeted electronic structures can be designed by altering the A, B, and X-site elements in the crystal structure, so that

other physical properties can be tailored, such as stability, light absorption, and charge migration [108]; (2) the unique energy band structures endow halide perovskites with suitable band edge positions to drive a broad range of photocatalytic reactions [109]; (3) the long carrier diffusion lengths and high charge mobility also render halide perovskites as promising candidates for the design of high-performance photocatalysts.

3.2. Halide Perovskites for Hydrogen Evolution

3.2.1. Pristine Halide Perovskites or Solid Solutions

As discussed above, the unique optoelectronic properties of halide perovskites are favourable to their application in photocatalytic reactions, including hydrogen evolution. The first milestone for photocatalytic hydrogen evolution using halide perovskites was reported by Park et al. [44]. As is known, most halide perovskites are unstable in polar solvents, especially water [87]. In order to conquer this, Park and his coworkers employed the dynamically balanced HI solution as the reaction medium, which can maintain the stability of MAPbI₃ (Figure 3a). MAPbI₃ is regarded as an ionic crystal consisting of MA⁺ and PbI₃⁻, which can be precipitated in saturated solutions. Hence, when MAPbI₃ precipitates are dissolved in saturated solution, they can be decomposed into MA⁺ and PbI₃⁻ ions. Simultaneously, MA⁺ and PbI₃⁻ ions were reprecipitated into crystals at the same rate. In this way, the MAPbI₃ powder could maintain stability in aqueous HI solution (Figure 3b). They also found out that different phases of MAPbI₃ can exist, depending on the concentrations of H⁺ and I⁻. However, only under the specific conditions of [I⁻] ≤ [H⁺], pH < -0.5, and -log [I⁻] < -0.4 can MAPbI₃ remain stable (Figure 3c). This pioneering work has opened up a way for using halide perovskites in photocatalytic fields. Afterward, Wang and his group elucidated the reaction mechanism of photocatalytic hydrogen evolution using MAPbI₃ [45]. In this reaction, MAPbI₃ played dual roles as a visible light photoabsorber and as a catalyst reductant. Meanwhile, both the Pb atoms and surface organic molecules participated in the reaction. First, an intermediate state of Pb—H was formed by the interaction between one H atom dissociated from an MA⁺ ion and Pb. Subsequently, H₂ was produced by the reaction of the Pb—H intermediate state with another H atom from an adjacent MA⁺ ion. The lost H would be replaced by protons from the solution to produce new MA⁺ ions through the Grotthuss mechanism.

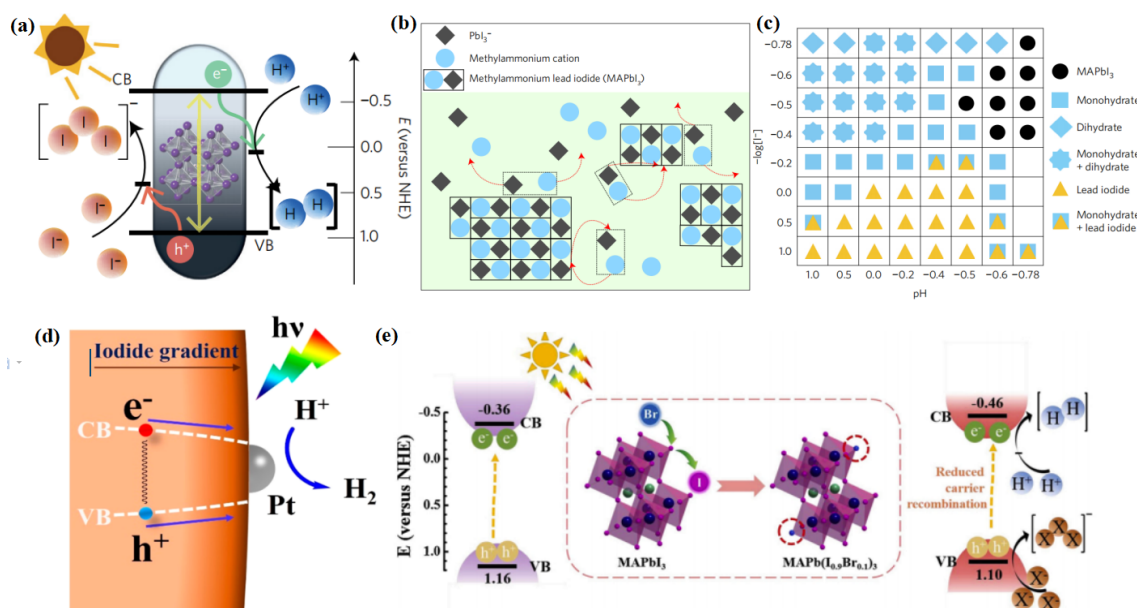


Figure 3. (a) Schematic energy band structure of MAPbI₃ powder for the photocatalytic HI splitting reaction. (b) Schematic illustration of the MAPbI₃ powder in dynamic equilibrium in saturated HI solution. The red color arrows represent dissociation and reprecipitation of MAPbI₃ crystal and ions.

(c) Constructed phase map as a function of $[I^-]$ and $[H^+]$. Each symbol represents the stable precipitate phases in saturated solutions at each $[I^-]$ and $[H^+]$ concentration. Main peaks of precipitated powder are not indexed under some conditions, expressed as empty boxes. (d) Promoted charge separation and enhanced photocatalytic H_2 evolution by formation of a bandgap funnel structure of $MAPbBr_{3-x}I_x$ near the surface. (e) Schematic band diagram of $MAPbI_3$ and $MAPb(I_{1-x}Br_x)_3$ ($x = 0.10$) crystal for photocatalytic HI splitting reaction. (a–c) Reproduced with permission [44]. Copyright: 2016, Nature Publishing Group. (d) Reproduced with permission [110]. Copyright: 2018, American Chemical Society. (e) Reproduced with permission [111]. Copyright: 2019, Elsevier.

As mentioned above, the CBM and VBM potentials of halide perovskites can be modified by modulating their compositions, which makes them suitable for gradient photocatalysis. By tuning the iodide concentration gradient, Huang et al. synthesized a mixed halide perovskite material ($MAPbBr_{3-x}I_x$) with a funnel-like bandgap structure [110]. The CBM becomes more positive with the increase of I concentration from the interior to the surface, whereas the VBM becomes more negative (Figure 3d). In this way, a smooth funnel is constructed, which promoted the charge transfer from the inside to the surface. As a consequence, this specially designed photocatalyst exhibited a H_2 generation rate of $255.3 \mu\text{mol h}^{-1}$. When Pt was further loaded on the surface of the perovskite, the photogenerated electrons on the perovskite surface transferred rapidly to the Pt particles, which further increased the H_2 generation rate to $651.2 \mu\text{mol h}^{-1}$. In a similar fashion, Huang's group also constructed a bandgap funnel-structured $CsPbBr_{3-x}I_x$ mixed halide perovskite via the graded distribution of iodide [112]. The obtained $CsPbBr_{3-x}I_x/Pt$ photocatalysts exhibited a H_2 evolution rate of $1120 \mu\text{mol g}^{-1} \text{h}^{-1}$ under visible light irradiation, along with a high stability during the 50 h of the photocatalytic experiment.

Considering the stability issues of halide perovskites, photocatalytic hydrogen generation using these materials are often conducted in HX ($X = \text{Cl}, \text{Br}, \text{or I}$) solution instead of direct water splitting [113]. Water splitting is a four-electron reaction, while the reduction of HI involves two electrons. When electrons drive the H_2 production reaction, I_3^- is generated during the photocatalytic process, which will darken the reaction medium gradually. As a consequence, the light absorption of the photocatalyst will be interfered. This can be overcome by the addition of hypophosphorus acid (H_3PO_2) as a chemical stabilizer, which can maintain the concentration of I^- and reduce the I_3^- ions [110]. Doping Br ions have also proved an effective way to enhance the photocatalytic HI splitting activity of $MAPbI_3$ [111]. The resultant $MAPb(I_{1-x}Br_x)_3$ perovskite exhibited a high H_2 evolution of $1471 \mu\text{mol h}^{-1} \text{g}^{-1}$ even without a Pt cocatalyst. This is because the addition of Br ions can tune the band structure of perovskite, with a negative shift of the CB potential, thus enhancing the reduction capability of electrons for efficient H_2 production (Figure 3e). In addition, the Br-incorporated perovskite has a lower H-Pb absorption energy, which makes it easier for H to transfer from MA^+ to the Pb atom at the defect site, thus increasing the H_2 evolution rate.

3.2.2. Halide Perovskite Composites

Wu et al. reported a $MAPbI_3/rGO$ composite with outstanding photocatalytic performance in aqueous HI solution (Figure 4a) [41]. It has a high H_2 evolution rate of $93.9 \mu\text{mol h}^{-1}$ under visible light irradiation, which is 67 times and 23 times higher than that of pristine $MAPbI_3$ and Pt-loaded $MAPbI_3$, respectively (Figure 4b). The remarkable performance could be attributed to the introduction of rGO, which possesses good charge transport ability and facilitates charge transfer. The electrons that transfer from $MAPbI_3$ to rGO then reduce protons to H_2 , resulting in excellent photocatalytic activity of the $MAPbI_3/rGO$ composite. Moreover, the composite is extremely stable, with no significant decrease of the H_2 evolution activity after 200 h of cyclic experiments (Figure 4c). As confirmed by XRD, the recycled photocatalyst showed no change or failure in structure. That was because the $MAPbI_3$ powders and the saturated HI solution were in dynamic equilibrium. When the reaction occurred, the exposed $MAPbI_3$ surface was restored all the time, ensuring the continuous oxidation of I^- to I_3^- on the surface in contact with HI.

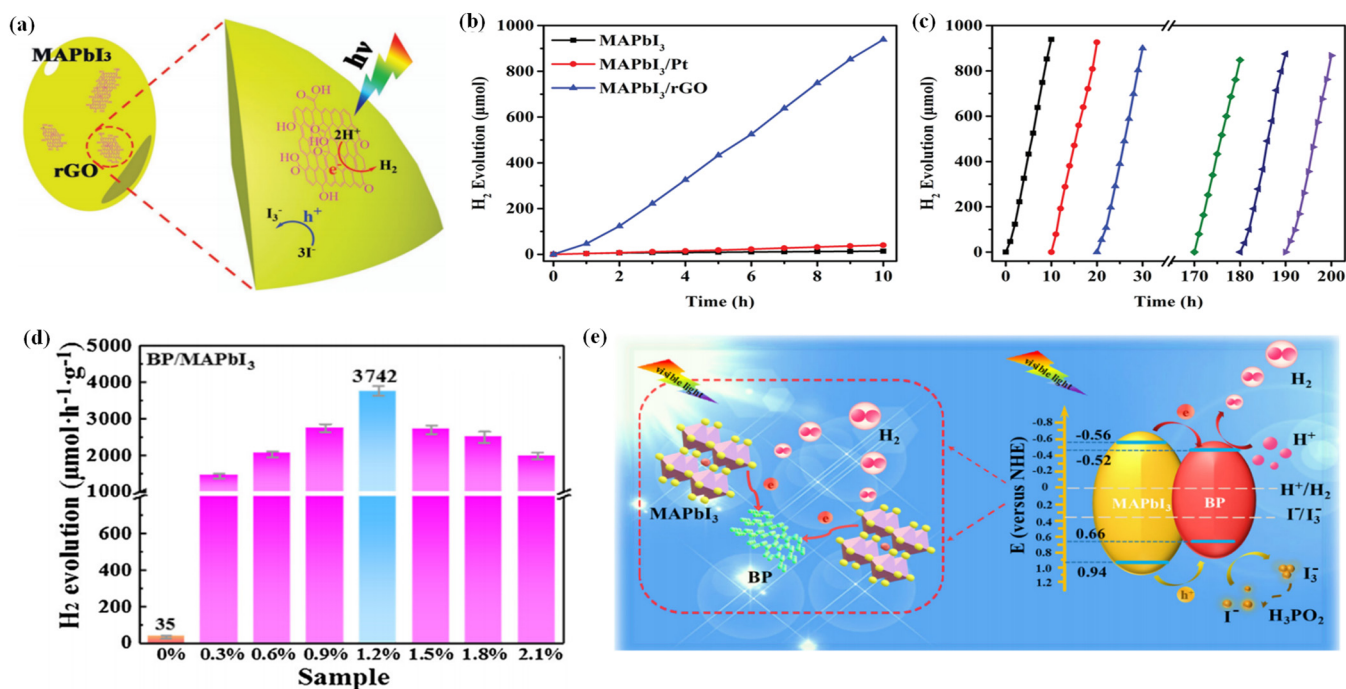


Figure 4. (a) Schematic illustration of photocatalytic H₂ evolution by MAPbI₃/rGO. (b) Comparison of the H₂ evolution performance of MAPbI₃, MAPbI₃/Pt, and MAPbI₃/rGO. (c) Stability test of MAPbI₃/rGO during 20 cycles of H₂ evolution experiments. Lines with different colors represent different cycles. (d) Photocatalytic H₂ evolution rates of BP/MAPbI₃. (e) Schematic mechanism of the photogenerated charge transfer in the BP/MAPbI₃ composite under visible light irradiation. (a–c) Reproduced with permission [41]. Copyright: 2018, Wiley. (d,e) Reproduced with permission [114]. Copyright: 2019, Elsevier.

Li et al. anchored a 2D few-layer black phosphorus (BP) on MAPbI₃ via electrostatic coupling and fabricated a BP/MAPbI₃ composite for photocatalytic hydrogen evolution [114]. The resultant BP/MAPbI₃ exhibited a superb photocatalytic hydrogen evolution rate of 3742 μmol h⁻¹ g⁻¹ under visible light, which was far higher than that of both pure MAPbI₃ and MAPbI₃/Pt (Figure 4d). Moreover, the BP/MAPbI₃ showed superior durability without no obvious decrease in the activity after 20 cycles. The outstanding photocatalytic activity and stability of the BP/MAPbI₃ could be attributed to the broadened light harvesting, enhanced charge separation, and high chemical/optical stability of BP/MAPbI₃ composite in HI solution (Figure 4e).

Wang et al. adopted a novel simultaneous dual-charge transportation modulation approach to improve the photocatalytic H₂ evolution activity of organic–inorganic MAPbBr₃ NCs [115]. They hybridized the MAPbBr₃ perovskite with Pt/Ta₂O₅ and poly(3,4-ethylene dioxothiophene):polystyrenesulfonate (PEDOT:PSS) nanoparticles, which acted as electron- and hole-transporting motifs, respectively. By providing new dual-charge transporting pathways, the charge separation and transportation efficiency of MAPbBr₃ was significantly improved. Tantalum pentoxide (Ta₂O₅) was selected for its ideal conduction band edge position, which can provide an electron transport pathway to accelerate the electron transportation from MAPbBr₃ (Figure 5a). Thus, Pt/Ta₂O₅-MAPbBr₃ contributed to the increase of H₂ evolution rate. PEDOT:PSS was used as an efficient hole-transporting material in the hybrid system for its more positive VBM than that of MAPbBr₃, which facilitated the Br-oxidation reaction (Figure 5b). Therefore, Pt/Ta₂O₅-MAPbBr₃-PEDOT:PSS was the most effective photocatalyst for H₂ evolution (Figure 5c). The photocatalytic hydrogen evolution rate on the hybridized system was increased by ca. 52 times than that of pristine MAPbBr₃, with an apparent quantum efficiency up to 16.4% at 420 nm.

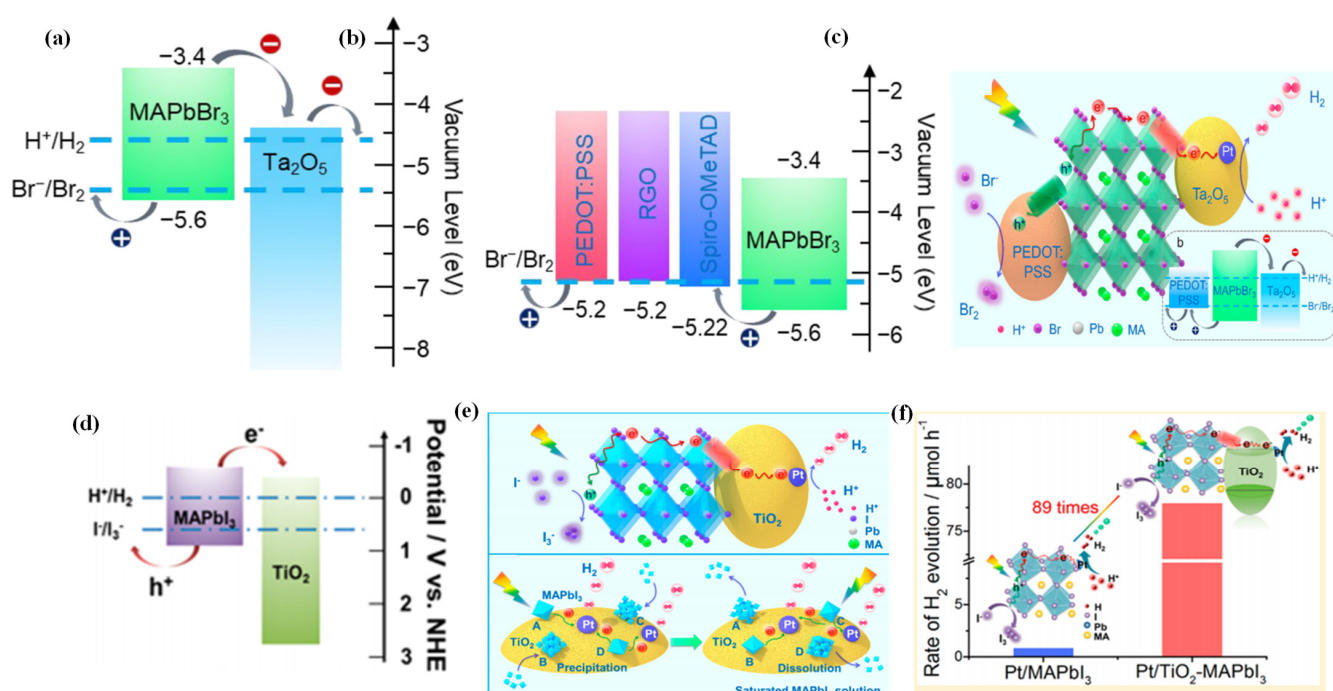


Figure 5. (a) Schematic energy levels of MAPbBr₃ and Ta₂O₅ and the redox potentials for HBr splitting reaction. (b) Energy level diagrams of MAPbBr₃ and hole-transporting materials. (c) Schematic illustration of the reaction mechanism for MAPbBr₃ with Pt/Ta₂O₅ and PEDOT:PSS as the electron- and hole-transporting channels, respectively. (d) Schematic diagrams of energy band of MAPbI₃ and TiO₂. (e) Schematic illustration of photocatalytic HI splitting for H₂ evolution by Pt/TiO₂-MAPbI₃ hybrid system under visible light irradiation. (f) Comparison of H₂ evolution activity over Pt/MAPbI₃ and Pt/TiO₂-MAPbI₃. (a–c) Reproduced with permission [115]. Copyright: 2019, American Chemical Society. (d–f) Reproduced with permission [42]. Copyright: 2018, American Chemical Society.

Through hybridization of MAPbI₃ with Pt/TiO₂, Wang et al. greatly enhanced the photocatalytic hydrogen evolution rate of MAPbI₃ from HI splitting [42]. Due to the suitable band alignment (Figure 5d), the TiO₂ nanoparticles can act as nanoscale electron-transporting channels, which allow efficient extraction of the photogenerated electrons from MAPbI₃. As illustrated in Figure 5e, the introduction of Pt/TiO₂ could create dynamically existing electron-transporting channels between the MAPbI₃ and Pt/TiO₂, which drastically enhanced the charge transportation efficiency of MAPbI₃ nanoparticles. As a consequence, the photocatalytic hydrogen evolution rate of Pt/TiO₂-MAPbI₃ was enhanced by ca. 89 times than that of Pt/MAPbI₃ (Figure 5f).

Wang et al. employed MoS₂ nanosheets as a cocatalyst to couple with MAPbI₃ and fabricated a MAPbI₃/MoS₂ composite for photocatalytic H₂ evolution [116]. Since the conduction band potential of MAPbI₃ is more negative than that of MoS₂, the photogenerated electrons can efficiently transfer from MAPbI₃ to MoS₂, which hindered the carrier recombination rates. As a result, the MAPbI₃/MoS₂ composite exhibited a H₂ evolution rate 121 times higher than pristine MAPbI₃.

3.2.3. Pb-Free Halide Perovskites

In order to overcome the toxicity of lead, Guo et al. developed an eco-friendly lead-free perovskite MA₃Bi₂I₉ and applied it for photocatalytic H₂ evolution [117]. Owing to the precipitation–solubility equilibrium reached in the system, the obtained MA₃Bi₂I₉ exhibited excellent phase stability in HI solution. After 70 h of repeated H₂ evolution, it showed no degradation or oxidation with satisfactory cycle stability. When using Pt as a cocatalyst,

the H_2 production rate was enhanced by 14 times compared with the pristine one, reaching $169.21 \mu\text{mol g}^{-1} \text{h}^{-1}$.

For the first time, Zhao et al. applied the $\text{Cs}_2\text{AgBiBr}_6$ (CABB) double perovskite for HBr splitting under visible light irradiation, in which RGO was introduced to extract the photogenerated electrons from CABB [118]. The resultant CABB/RGO composite exhibited a H_2 evolution of $489 \mu\text{mol g}^{-1}$ within 10 h under visible light irradiation, which was 80 times higher than that of bare CABB. Moreover, the CABB/RGO composite with optimal RGO demonstrated ideal stability, with no significant decline in H_2 evolution after 120 h continuous photocatalytic reaction. As confirmed by the photoluminescence (PL) (Figure 6a) and photoelectrochemical measurements (Figure 6b), the CABB/RGO composite exhibited suppressed charge recombination and better charge transfer ability than bare CABB. This could be attributed to the introduction of conductive RGO, which could accelerate the electron transfer from CABB through the M-O-C bonds. Subsequently, the transferred electrons reduce H^+ to generate H_2 at the active sites of RGO, while the holes on CABB particles oxidized Br^- to produce Br_3^- (Figure 6c).

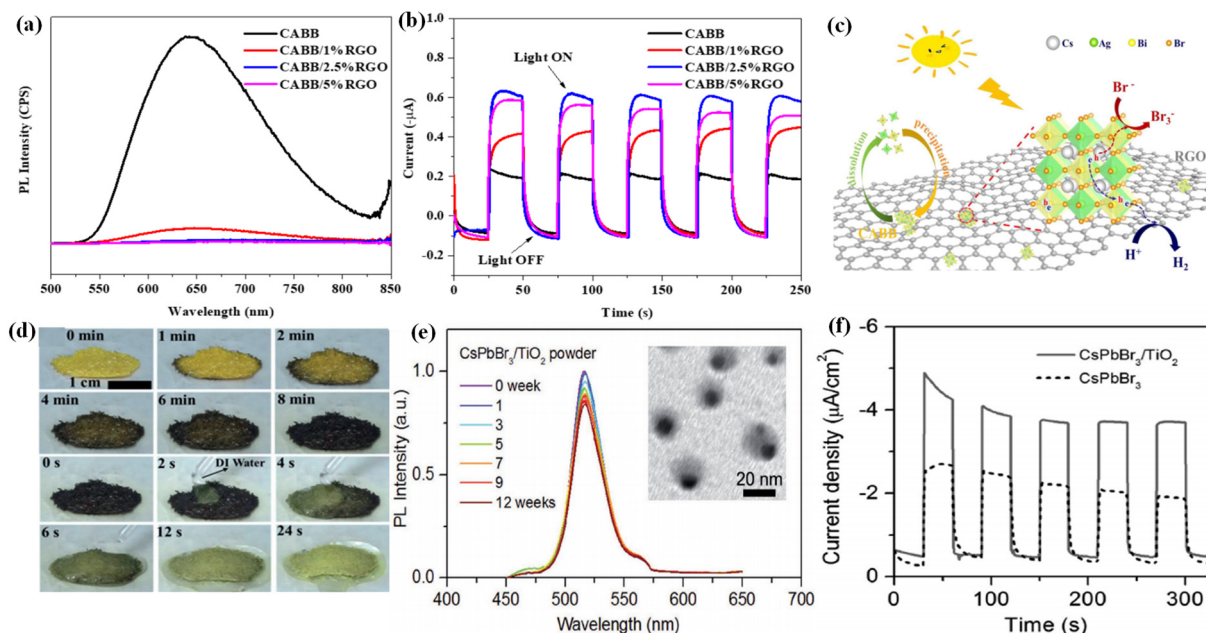


Figure 6. (a) Steady-state PL spectra of the CABB/xRGO composites ($x = 0, 1\%, 2.5\%, 5\%$). (b) Photocurrent responses of the CABB/xRGO samples ($x = 0, 1\%, 2.5\%, 5\%$) recorded at 0 V vs. Ag/AgCl electrode. (c) Schematic mechanism of photocatalytic HBr splitting by CABB/RGO under visible light irradiation. (d) In situ observation of the reversible DMASnI_3 transformation process at 80°C in air. (e) The relative PL intensity of $\text{CsPbBr}_3/\text{TiO}_2$ NCs after immersing in Milli-Q water (0–12 weeks). Inset: TEM image of $\text{CsPbBr}_3/\text{TiO}_2$ NCs after immersing in Milli-Q water for 12 weeks. (f) Transient photocurrent responses of CsPbBr_3 and $\text{CsPbBr}_3/\text{TiO}_2$ NCs electrodes at -0.1 V versus NHE. (a–c) Reproduced with permission [118]. Copyright: 2020, Elsevier. (d) Reproduced with permission [119]. Copyright: 2018, Wiley. (e,f) Reproduced with permission [120]. Copyright: 2018, Wiley.

3.2.4. Water Stable Halide Perovskites

In order to overcome the stability issues of most halide perovskites, Ju et al. developed a lead-free hybrid perovskite single-crystal DMASnI_3 ($\text{DMA} = \text{CH}_3\text{NH}_2\text{CH}^+$) with excellent water phase stability [119]. No decomposition was observed when DMASnI_3 was immersed in deionized water for 16 h. Inspired by this, they applied DMASnI_3 as a photocatalyst for H_2 evolution in deionized water. A H_2 evolution rate of $0.64 \mu\text{mol h}^{-1}$ was observed on the DMASnI_3 crystals, accompanied by good recycling properties. Interestingly, the DMASnI_3 crystals exhibited a reversible band gap narrowing behavior without phase transformation. When exposed to deionized water, the transformed samples

in black can self-heal into yellow ones rapidly (Figure 6d). The narrow band gap, high stability, as well as outstanding electrical properties render DMASnI₃ as a promising optoelectronic material. By the encapsulation of colloidal CsPbBr₃ NCs into the TiO₂ shell, Li et al. obtained nearly monodispersed CsPbBr₃/TiO₂ core/shell NCs with excellent water stability [120]. The size, structure, morphology, and optical properties remained identical after the CsPbBr₃/TiO₂ core/shell NCs were immersed in water for three months (Figure 6e), representing one of the most water-stable inorganic shell passivated perovskite NCs. Moreover, owing to the electrical conductivity of the TiO₂ shell, the CsPbBr₃/TiO₂ core/shell NCs exhibited increased charge separation efficiency (Figure 6f), making it a potential material for optoelectronic and photocatalytic applications in aqueous phase. The photocatalytic performance of halide perovskite-based systems for hydrogen generation is summarized in Table 1.

Table 1. Summary of photocatalytic hydrogen evolution activity of halide perovskite-based systems.

Photocatalyst	Solution	Light Source	Activity ($\mu\text{mol g}^{-1} \text{h}^{-1}$)	Stability (h)	Ref.
MAPbI ₃ /Pt	Aqueous HI	visible light ($\lambda \geq 475 \text{ nm}$)	57	160	[44]
MAPbI _{3-x} Br _x /Pt	Aqueous HBr/HI	visible light ($\lambda \geq 420 \text{ nm}$)	2604	>30	[110]
Pt/TiO ₂ -MAPbI ₃	Aqueous HI	visible light ($\lambda \geq 420 \text{ nm}$)	77.9	>12	[42]
MAPbI ₃ /rGO	Aqueous HI	visible light ($\lambda \geq 420 \text{ nm}$)	939	200	[41]
BP/MAPbI ₃	Aqueous HI	visible light ($\lambda \geq 420 \text{ nm}$)	3472	200	[114]
PEDOT:PSS/MAPbBr ₃ /Ta ₂ O ₅	Aqueous HBr	visible light ($\lambda \geq 420 \text{ nm}$)	1050	>4	[115]
MAPbI ₃ /MoS ₂	Aqueous HI	white LED lamp (450 nm)	1963	>24	[116]
MA ₃ Bi ₂ I ₉ /Pt	Aqueous HI	visible light ($\lambda \geq 400 \text{ nm}$)	170	70	[117]
CsPbBr _{3-x} I _x /Pt	Aqueous HBr/HI	visible light ($\lambda \geq 420 \text{ nm}$)	1120	>50	[113]
Cs ₂ AgBiBr ₆ /rGO	Aqueous HBr	visible light ($\lambda \geq 420 \text{ nm}$)	48.9	120	[118]
DMASnI ₃	DI water	300 W Xe lamp (full spectrum)	3.2	>5	[119]
Ni ₃ C/MAPbI ₃	Aqueous HI	visible light ($\lambda \geq 420 \text{ nm}$)	2362	>100	[121]
MAPbI ₃ /CoP	Aqueous HI	visible light ($\lambda \geq 420 \text{ nm}$)	2087.5	27	[122]
Pt-DA ₃ BiI ₆	Aqueous HI	100 W white LED lamp	91	>16	[123]
MA ₃ Bi ₂ I ₉ /DMA ₃ BiI ₆	Aqueous HI	visible light ($\lambda \geq 420 \text{ nm}$)	198.4	>90	[124]
MA ⁺ -crafted MAPbI ₃	Aqueous HI	visible light ($\lambda \geq 420 \text{ nm}$)	313	–	[125]
ML-MoS ₂ /MAPbI ₃ -MC	Aqueous HI	visible light ($\lambda \geq 420 \text{ nm}$)	13,600	208	[126]
MoS ₂ /M _{0.6} F _{0.4} PbI ₃	Aqueous HI	visible light ($\lambda \geq 420 \text{ nm}$)	2131	>90	[127]
PtI _x /[(CH ₃) ₂ NH ₂] ₃ [BiI ₆]	Aqueous HI	Commercial LED lamp, $\lambda = 425 \text{ nm}$	94	100	[128]

4. Conclusions and Prospects

In this review, we have introduced the recent advances made in the field of halide perovskite-based hydrogen evolution, focusing on the strategies to enhance the photocatalytic activity of these materials. Although halide perovskites have intriguing properties, their poor stabilities arising from the soft ionic crystal structures restrict their application in photocatalysis. However, via intrinsically improving the crystal stabilities of halide perovskites, several “stable” photocatalytic systems based on these kind of materials have been designed [119,120]. Moreover, by altering the external reaction conditions, such as using saturated halo acid solutions as the solvent, halide perovskites have been successfully used in photocatalytic hydrogen evolution [41,42,44,114–119,121–128]. In spite of this, there are still big challenges when applying halide perovskites in photocatalytic reactions under more common environments. On the basis of the current level of knowledge and the limitations of halide perovskites, some promising approaches to enhance the activity and stability of halide perovskite-based photocatalysis are proposed.

4.1. Improving the Long-Term Catalytic Stability of Halide Perovskites

Although conducting photocatalytic reactions in halo acid solutions have been proven effective for hydrogen evolution, such methods are not universal in nature. To limit contact between halide perovskites and the polar solvent, it is essential to explore excellent sealing technology to secure the stability of halide perovskites. There are two essential criteria to be considered when establishing this technology: one is the transparency of the sealing materials which can ensure sufficient light absorption of halide perovskites. The second criterion is the good conductivity of the sealing material that can allow the effective extraction of photo-generated carriers. At present, transparent resin (epoxy) is the most commonly used sealing material. Conductive carbon paste is also employed as the sealing agent in some studies, considering its conductive property and higher resistance towards degradation. Alternatively, some researchers encapsulate halide perovskites with electron- and hole-transport materials together to fabricate corresponding photoelectrodes for photocatalysis. In addition, halide perovskites can be separated from the polar solvent by encapsulating the perovskite layer in a solar cell structure to develop a PV-PEC reaction system. This system has the advantage of increased redox capacity of the PEC cell owing to the photovoltaic device, which allows larger voltage in series and thus supporting a wide range of applications.

4.2. Improving the H₂ Generation Activity of Halide Perovskite-Based Photocatalysts

As shown in Table 1, the highest H₂ evolution rate so far achieved for halide perovskite-based photocatalyst is about 13.6 mmol g⁻¹ h⁻¹ [126]. Although great achievements have been reached, the present H₂ evolution rate of this kind of material is far from practical application. There are several strategies proposed to further improve the H₂ evolution activity of halide perovskites: the first approach is the controllable synthesis of nanostructures with definite morphologies such as nanosheets, nanoplatelets to afford more exposed surfaces, and to increase the surface area and provide more active sites. Another option is the combination of single-atom catalysis with halide perovskites. Owing to the rapid increase of surface-free energy, quantum confinement effects, unsaturated coordination, and interactions between the metal with reduced size and substrate, the catalytic activity and stability of halide perovskites can be improved [43]. The construction of novel heterojunctions between halide perovskites and a suitable charge-transporting motif with desirable/well matching band alignment can enhance the charge separation [129]. For example, by coupling halide perovskites with electron- or hole-transporting materials such as GO, rGO, MXene, MOF, etc., can effectively promote charge separation and migration, thereby resulting in efficient catalytic activity. Type-II and Z-scheme are the most widely reported heterojunctions to achieve rapid charge transfer.

4.3. Enhance the Redox Ability of Halide Perovskites

The relatively narrow bandgaps of halide perovskites, which are especially associated with the VB edges, will inevitably bring about poor oxidation abilities. The weak oxidation capacity of halide perovskites will limit their application in some oxidation reactions—for instance, water oxidation (H₂O/O₂ at 1.23 eV vs. RHE) and organic compound mineralization (OH⁻/•OH at 1.67 eV vs. RHE). The combination of halide perovskites with other semiconductors with more positive VB (building a Z-scheme heterojunction) can achieve strong redox capabilities, broad light absorption, and efficient charge separation. Alternatively, by encapsulating the perovskite layer in a solar cell architecture to develop a perovskite-based PEC reaction system, the redox ability of perovskite can be enhanced by the applied voltage to achieve a broad reaction scope [43].

4.4. Exploring Mechanisms of Perovskite-Based Photocatalysis by Combining Experimental and Theoretical Research

Despite the great progress made in perovskite-based photocatalysis, there is a lack of comprehensive understanding of reaction mechanisms, such as the catalytic kinetic

processes, the photophysical processes, and microscopic mechanisms of the involved surface chemical reactions. Hence, a complete theoretical model is required to interpret the roles of perovskite materials in photocatalytic redox reactions. Theoretical studies can not only help to enhance the understanding of established activities, but also can provide guidance for developing more efficient photocatalysts for redox reactions. By combining theoretical calculations and in-situ characterization techniques, mechanisms of perovskite-based photocatalysis such as reaction pathways and changes of catalysts during photocatalysis can be probed.

In this review, we introduced up-to-date progress of halide perovskites in photocatalytic hydrogen production. Up to this stage, perovskite powder (photocatalysis) and thin film (PEC and PV-PEC)-based photocatalysis systems have been proved to be effective for solar fuel production. However, from the viewpoint of commercialization, the factors of yield, reaction kinetics, stability, scalability, and cost and simplicity of production shall be reassessed. In addition, the general photocatalytic activity and stability of perovskite-based materials are currently far from optimal, and their application in photocatalysis is still in its infancy. The use of perovskites to address energy and environmental concerns still faces many challenges. These challenges also imply large opportunities for further exploration of perovskite-based photocatalysts with improved activity and more potential reactions. We hope that this review can provide some guidance toward finding optimal performance and stability for perovskite-based photocatalytic applications.

Author Contributions: Z.Z. wrote and formatted the review. R.Z., D.L. and Y.J. significantly contributed to the writing and preparation of tables and figures. X.W. and H.T. contextualized and structured the manuscript. J.X. reviewed and supervised the present manuscript. All authors have read and agreed to the published version of the manuscript.

Funding: This work was financially supported by the National Natural Science Foundation of China (51972213), Natural Science Foundation of Shanghai (22ZR1460700), and Shanghai Institute of Technology (XTCX2022–28).

Institutional Review Board Statement: Not applicable.

Informed Consent Statement: Not applicable.

Conflicts of Interest: The authors declare no conflict of interest.

References

1. Lu, Y.; Yin, W.J.; Peng, K.L.; Wang, K.; Hu, Q.; Selloni, A.; Chen, F.R.; Liu, L.M.; Sui, M.L. Self-hydrogenated shell promoting photocatalytic H₂ evolution on anatase TiO₂. *Nat. Commun.* **2018**, *9*, 2752. [[CrossRef](#)] [[PubMed](#)]
2. Cheng, C.; He, B.; Fan, J.; Cheng, B.; Cao, S.; Yu, J. An inorganic/organic S-scheme heterojunction H₂-production photocatalyst and its charge transfer mechanism. *Adv. Mater.* **2021**, *33*, 2100317. [[CrossRef](#)]
3. Liu, S.; Kuang, W.; Meng, X.; Qi, W.; Adimi, S.; Guo, H.; Guo, X.; Pervaiz, E.; Zhu, Y.; Xue, D.; et al. Dual-phase metal nitrides as highly efficient co-catalysts for photocatalytic hydrogen evolution. *Chem. Eng. J.* **2021**, *416*, 129116. [[CrossRef](#)]
4. Chen, S.; Takata, T.; Domen, K. Particulate photocatalysts for overall water splitting. *Nat. Rev. Mater.* **2017**, *2*, 17050. [[CrossRef](#)]
5. Wang, Q.; Domen, K. Particulate photocatalysts for light-driven water splitting: Mechanisms, challenges, and design strategies. *Chem. Rev.* **2020**, *120*, 919–985. [[CrossRef](#)]
6. Fujishima, A.; Honda, K. Electrochemical photolysis of water at a semiconductor electrode. *Nature* **1972**, *238*, 37–38. [[CrossRef](#)]
7. Liu, J.W.; Zhang, L.; Sun, Y.F.; Luo, Y. Bifunctional Ag-decorated CeO₂ nanorods catalysts for promoted photodegradation of methyl orange and photocatalytic hydrogen evolution. *Nanomaterials* **2021**, *11*, 1104. [[CrossRef](#)]
8. Rayalu, S.S.; Jose, D.; Mangrulkar, P.A.; Joshi, M.; Hippargi, G.; Shrestha, K.; Klabunde, K. Photodeposition of AuNPs on metal oxides: Study of SPR effect and photocatalytic activity. *Int. J. Hydrog. Energy* **2014**, *309*, 3617–3624. [[CrossRef](#)]
9. Ma, X.H.; Liu, Y.N.; Wang, Y.P.; Jin, Z.L. Co₃O₄/CeO₂ p-n heterojunction construction and application for efficient photocatalytic hydrogen evolution. *Int. J. Hydrog. Energy* **2021**, *46*, 33809–33822. [[CrossRef](#)]
10. Jin, Z.L.; Li, T.; Wang, K.; Guo, X. Interface engineering: Synergism between S-scheme heterojunctions and Mo-O bonds for promote photocatalytic hydrogen evolution. *Colloid. Interface Sci.* **2022**, *609*, 212–223. [[CrossRef](#)]
11. Tahir, M.B.; Sagir, M.; Abas, N. Enhanced photocatalytic performance of CdO-WO₃ composite for hydrogen production. *Int. J. Hydrog. Energy* **2019**, *44*, 24690–24697. [[CrossRef](#)]
12. Jineesh, P.; Bhagya, T.C.; Remya, R.; Shibli, S.M.A. Photocatalytic hydrogen generation by WO₃ in synergism with hematite-anatase heterojunction. *Int. J. Hydrog. Energy* **2020**, *45*, 18946–18960. [[CrossRef](#)]

13. Li, T.; Guo, X.; Zhang, L.J.; Yan, T.; Jin, Z.L. 2D CoP supported 0D WO₃ constructed S-scheme for efficient photocatalytic hydrogen evolution. *Int. J. Hydrog. Energy* **2021**, *46*, 20560–20572. [[CrossRef](#)]
14. Zhang, J.X.; Wang, Y.D.; Dong, H.; Zhou, X. Theoretical investigation of loading Ni clusters on the alpha-Ga₂O₃ surfaces for photocatalytic hydrogen evolution. *J. Energy Chem.* **2019**, *30*, 8–18. [[CrossRef](#)]
15. Yoon, H.J.; Yang, J.H.; Park, S.J.; Rhee, C.K.; Sohn, Y. Photocatalytic CO₂ reduction and hydrogen production over Pt/Zn-embedded beta-Ga₂O₃ nanorods. *Appl. Surf. Sci.* **2021**, *536*, 147753. [[CrossRef](#)]
16. Zhang, X.Y.; Zhang, Z.Z.; Huang, H.J.; Wang, Y.; Tong, N.; Lin, J.J.; Liu, D.; Wang, X.X. Oxygen vacancy modulation of two-dimensional-Ga₂O₃ nanosheets as efficient catalysts for photocatalytic hydrogen evolution. *Nanoscale* **2018**, *10*, 21509–21517. [[CrossRef](#)]
17. Han, C.Q.; Mao, W.T.; Bao, K.Y.; Xie, H.Q.; Jia, Z.Y.; Ye, L.Q. Preparation of Ag/Ga₂O₃ nanofibers via electrospinning and enhanced photocatalytic hydrogen evolution. *Int. J. Hydrog. Energy* **2017**, *42*, 19913–19919. [[CrossRef](#)]
18. Li, F.H.; Yang, J.B.; Gao, J.P.; Liu, Y.; Gong, Y.L. Enhanced photocatalytic hydrogen production of CdS embedded in cationic hydrogel. *Int. J. Hydrog. Energy* **2020**, *45*, 1969–1980. [[CrossRef](#)]
19. Zhang, G.X.; Guan, Z.J.; Yang, J.J.; Li, Q.Y.; Zhou, Y.; Zou, Z.G. Metal sulfides for photocatalytic hydrogen production: Current development and future challenges. *Solar RRL* **2022**, *6*, 2200587. [[CrossRef](#)]
20. Ding, C.; Zhao, C.X.; Cheng, S.; Yang, X.F. Ultrahigh photocatalytic hydrogen evolution performance of coupled 1D CdS/1T-phase dominated 2D WS₂ nanoheterojunctions. *Chin. J. Catal.* **2022**, *43*, 403–409. [[CrossRef](#)]
21. Yuan, M.; Zhou, W.H.; Kou, D.X.; Zhou, Z.J.; Meng, Y.N.; Wu, S.X. Cu₂ZnSnS₄ decorated CdS nanorods for enhanced visible-light-driven photocatalytic hydrogen production. *Int. J. Hydrog. Energy* **2018**, *43*, 20408–20416. [[CrossRef](#)]
22. Yang, W.; Xu, M.; Tao, K.Y.; Zhang, J.H.; Zhong, D.C.; Lu, T.B. Building 2D/2D CdS/MOLs heterojunctions for efficient photocatalytic hydrogen evolution. *Small* **2022**, *18*, 2200332. [[CrossRef](#)] [[PubMed](#)]
23. Zhang, F.J.; Li, X.; Sun, X.Y.; Kong, C.; Xie, W.J.; Li, Z.; Liu, J. Surface partially oxidized MoS₂ nanosheets as a higher efficient cocatalyst for photocatalytic hydrogen production. *Appl. Surf. Sci.* **2019**, *487*, 734–742. [[CrossRef](#)]
24. Nagajyothi, P.C.; Devarayapalli, K.C.; Shim, J.; Vattikuti, S.V.P. Highly efficient white-LED-light-driven photocatalytic hydrogen production using highly crystalline ZnFe₂O₄/MoS₂ nanocomposites. *Int. J. Hydrog. Energy* **2020**, *45*, 32756–32769. [[CrossRef](#)]
25. Wang, X.W.; Yuan, B.; Xie, Z.H.; Wang, D.X.; Zhang, R.B. ZnS-CdS/Graphene oxide heterostructures prepared by a light irradiation-assisted method for effective photocatalytic hydrogen generation. *Colloid. Interface Sci.* **2015**, *446*, 150–154. [[CrossRef](#)]
26. Dong, J.; Fang, W.J.; Yuan, H.; Xia, W.W.; Zeng, X.H.; Shangguan, W.F. Few-layered MoS₂/ZnCdS/ZnS heterostructures with an enhanced photocatalytic hydrogen evolution. *ACS Appl. Energy Mater.* **2022**, *5*, 4893–4902. [[CrossRef](#)]
27. Chang, C.J.; Chu, K.W.; Hsu, M.H.; Chen, C.Y. Ni-doped ZnS decorated graphene composites with enhanced photocatalytic hydrogen-production performance. *Int. J. Hydrog. Energy* **2015**, *40*, 14498–14506. [[CrossRef](#)]
28. Jian, L.; Zhang, H.Z.; Liu, B.; Pan, C.S.; Dong, Y.M.; Wang, G.L.; Zhong, J.; Zheng, Y.J.; Zhu, Y.F. Monodisperse Ni-clusters anchored on carbon nitride for efficient photocatalytic hydrogen evolution. *Chin. J. Catal.* **2022**, *43*, 536–545. [[CrossRef](#)]
29. Du, J.; Li, S.M.; Du, Z.G.; Meng, S.M.; Li, B. Boron/oxygen-codoped graphitic carbon nitride nanomesh for efficient photocatalytic hydrogen evolution. *Chem. Eng. J.* **2021**, *407*, 127114. [[CrossRef](#)]
30. Zhang, J.H.; Wei, M.J.; Wei, Z.W.; Pan, M.; Su, C.Y. Ultrathin graphitic carbon nitride nanosheets for photocatalytic hydrogen evolution. *ACS Appl. Nano Mater.* **2020**, *3*, 1010–1018. [[CrossRef](#)]
31. Jiang, Y.; Qu, F.Q.; Tian, L.; Yang, X.F.; Zou, Z.Y.; Lin, Z.X. Self-assembled g-C₃N₄ nanoarchitectures with boosted photocatalytic solar-to-hydrogen efficiency. *Appl. Surf. Sci.* **2019**, *487*, 59–67. [[CrossRef](#)]
32. Lu, Y.F.; Wang, W.S.; Cheng, H.R.; Qiu, H.J.; Sun, W.H.; Fang, X.; Zhu, J.F.; Zheng, Y.H. Bamboo-charcoal-loaded graphitic carbon nitride for photocatalytic hydrogen evolution. *Int. J. Hydrog. Energy* **2022**, *47*, 3733–3740. [[CrossRef](#)]
33. Xu, H.T.; Xiao, R.; Huang, J.R.; Jiang, Y.; Zhao, C.X.; Yang, X.F. In situ construction of protonated g-C₃N₄/Ti₃C₂ MXene Schottky heterojunctions for efficient photocatalytic hydrogen production. *Chin. J. Catal.* **2021**, *42*, 107–114. [[CrossRef](#)]
34. Xu, Y.F.; Yang, M.Z.; Chen, B.X.; Wang, X.D.; Chen, H.Y.; Kuang, D.B.; Su, C.Y. A CsPbBr₃ perovskite quantum dot/graphene oxide composite for photocatalytic CO₂ reduction. *J. Am. Chem. Soc.* **2017**, *139*, 5660–5663. [[CrossRef](#)]
35. Zhang, Z.J.; Jiang, Y.; Shu, M.Y.; Li, L.; Dong, Z.L.; Xu, J.Y. Artificial photosynthesis over metal halide perovskites: Achievements, challenges, and prospects. *J. Phys. Chem. Lett.* **2021**, *12*, 5864–5870. [[CrossRef](#)]
36. Li, L.; Zhang, Z.J.; Ding, C.; Xu, J.Y. Boosting charge separation and photocatalytic CO₂ reduction of CsPbBr₃ perovskite quantum dots by hybridizing with P3HT. *Chem. Eng. J.* **2021**, *419*, 129543. [[CrossRef](#)]
37. Ou, M.; Tu, W.G.; Yin, S.M.; Xing, W.N.; Wu, S.Y.; Wang, H.J.; Wan, S.P.; Zhong, Q.; Xu, R. Amino-assisted anchoring of CsPbBr₃ perovskite quantum dots on porous g-C₃N₄ for enhanced photocatalytic CO₂ reduction. *Angew. Chem. Int. Ed.* **2018**, *57*, 13570–13574. [[CrossRef](#)]
38. Chen, Z.; Hu, Y.; Wang, J.; Shen, Q.; Zhang, Y.; Ding, C.; Bai, Y.; Jiang, G.; Li, Z.; Gaponik, N. Boosting photocatalytic CO₂ reduction on CsPbBr₃ perovskite nanocrystals by immobilizing metal complexes. *Chem. Mater.* **2020**, *32*, 1517–1525. [[CrossRef](#)]
39. Jiang, Y.; Wang, Y.T.; Zhang, Z.J.; Dong, Z.L.; Xu, J.Y. 2D/2D CsPbBr₃/BiOCl heterojunction with an S-scheme charge transfer for boosting the photocatalytic conversion of CO₂. *Inorg. Chem.* **2022**, *61*, 10557–10566. [[CrossRef](#)]
40. Dong, Z.L.; Zhou, J.X.; Zhang, Z.J.; Jiang, Y.; Zhou, R.; Yao, C.X. Construction of a p–n type S-scheme heterojunction by incorporating CsPbBr₃ nanocrystals into mesoporous Cu₂O microspheres for efficient CO₂ photoreduction. *ACS Appl. Energy Mater.* **2022**, *5*, 10076–10085. [[CrossRef](#)]

41. Wu, Y.; Wang, P.; Zhu, X.; Zhang, Q.; Wang, Z.; Liu, Y.; Zou, G.; Dai, Y.; Whangbo, M.; Huang, B. Composite of $\text{CH}_3\text{NH}_3\text{PbI}_3$ with reduced graphene oxide as a highly efficient and stable visible-light photocatalyst for hydrogen evolution in aqueous HI solution. *Adv. Mater.* **2018**, *30*, 1704342. [[CrossRef](#)] [[PubMed](#)]
42. Wang, X.; Wang, H.; Zhang, H.; Yu, W.; Wang, X.; Zhao, Y.; Zong, X.; Li, C. Dynamic interaction between methylammonium lead iodide and TiO_2 nanocrystals leads to enhanced photocatalytic H_2 evolution from HI splitting. *ACS Energy Lett.* **2018**, *3*, 1159–1164. [[CrossRef](#)]
43. Yuan, J.; Liu, H.L.; Wang, S.R.; Li, X.G. How to apply metal halide perovskites to photocatalysis: Challenges and development. *Nanoscale* **2021**, *13*, 10281–10304. [[CrossRef](#)] [[PubMed](#)]
44. Park, S.; Chang, W.J.; Lee, C.W.; Park, S.; Ahn, H.-Y.; Nam, K.T. Photocatalytic hydrogen generation from hydriodic acid using methylammonium lead iodide in dynamic equilibrium with aqueous solution. *Nat. Energy* **2016**, *2*, 16185. [[CrossRef](#)]
45. Wang, L.; Xiao, H.; Cheng, T.; Li, Y.Y.; Goddard, W.A. Pb-Activated amine-assisted photocatalytic hydrogen evolution reaction on organic-inorganic perovskites. *J. Am. Chem. Soc.* **2018**, *140*, 1994–1997. [[CrossRef](#)]
46. Gao, G.; Xi, Q.Y.; Zhou, H.; Zhao, Y.X.; Wu, C.Q.; Wang, L.D.; Guo, P.R.; Xu, J.W. Novel inorganic perovskite quantum dots for photocatalysis. *Nanoscale* **2017**, *9*, 12032–12038. [[CrossRef](#)]
47. Cardenas-Morcoso, D.; Gualdrón-Reyes, A.F.; Ferreira Vitoreti, A.B.; GarcíaTecedor, M.; Yoon, S.J.; Solís de la Fuente, M. Photocatalytic and photoelectrochemical degradation of organic compounds with allinorganic metal halide perovskite quantum dots. *J. Phys. Chem. Lett.* **2019**, *10*, 630–636. [[CrossRef](#)]
48. Zhang, Z.; Liang, Y.; Huang, H.; Liu, X.; Li, Q.; Chen, L. Stable and highly efficient photocatalysis with lead-free double-perovskite of $\text{Cs}_2\text{AgBiBr}_6$. *Angew. Chem. Int. Ed.* **2019**, *58*, 7263–7267. [[CrossRef](#)]
49. Feng, X.; Ju, H.; Song, T.; Fang, T.; Liu, W.; Huang, W. Highly efficient photocatalytic degradation performance of $\text{CsPb}(\text{Br}_{1-x}\text{Cl}_x)_3$ -Au nanoheterostructures. *ACS Sustain. Chem. Eng.* **2019**, *7*, 5152–5156. [[CrossRef](#)]
50. Shu, M.Y.; Lu, J.L.; Zhang, Z.J.; Shen, T.; Xu, J.Y. CsPbBr_3 Perovskite quantum dots/ultrathin C_3N_4 nanosheet 0D/2D composite: Enhanced stability and photocatalytic activity. *J. Inorg. Mater.* **2021**, *36*, 1217–1222. [[CrossRef](#)]
51. Xiao, X.; Guo, S.K.; Ding, C.; Zhang, Z.J.; Huang, H.R.; Xu, J.Y. CsPbBr_3 @ TiO_2 core-shell structure nanocomposite as a water stable and efficient visible-light-driven photocatalyst. *J. Inorg. Mater.* **2021**, *36*, 507–512. [[CrossRef](#)]
52. Schunemann, S.; Gastel, M.; Tuysuz, H. A CsPbBr_3 / TiO_2 composite for visible-light-driven photocatalytic benzyl alcohol oxidation. *ChemSusChem* **2018**, *11*, 2057–2061. [[CrossRef](#)] [[PubMed](#)]
53. Huang, H.; Yuan, H.; Janssen, K.; Solís-Fernández, G.; Wang, Y.; Tan, C.; Jonckheere, D.; Debroye, E.; Long, J.; Hendrix, J.; et al. Efficient and selective photocatalytic oxidation of benzylic alcohols with hybrid organic-inorganic perovskite materials. *ACS Energy Lett.* **2018**, *3*, 755–759. [[CrossRef](#)]
54. Zhu, X.; Lin, Y.; Sun, Y.; Beard, M.; Yan, Y. Lead-halide perovskites for photocatalytic α -alkylation of aldehydes. *J. Am. Chem. Soc.* **2019**, *141*, 733–738. [[CrossRef](#)]
55. Zhu, X.; Lin, Y.; San Martin, J.; Sun, Y.; Zhu, D.; Yan, Y. Lead halide perovskites for photocatalytic organic synthesis. *Nat. Commun.* **2019**, *10*, 2843. [[CrossRef](#)]
56. Jeon, N.J.; Noh, J.H.; Yang, W.S.; Kim, Y.C.; Ryu, S.; Seo, J.; Seok, S.I. Compositional engineering of perovskite materials for high-performance solar cells. *Nature* **2015**, *517*, 476–480. [[CrossRef](#)]
57. Fu, Y.; Zhu, H.; Chen, J.; Hautzinger, M.P.; Zhu, X.Y.; Jin, S. Metal halide perovskite nanostructures for optoelectronic applications and the study of physical properties. *Nat. Rev. Mater.* **2019**, *4*, 169–188. [[CrossRef](#)]
58. Kulkarni, S.A.; Baikie, T.; Boix, P.P.; Yantara, N.; Mathews, N.; Mhaisalkar, S. Band-gap tuning of lead halide perovskites using a sequential deposition process. *J. Mater. Chem. A* **2014**, *2*, 9221–9225. [[CrossRef](#)]
59. Nedelcu, L.G.; Protesescu, S.; Yakunin, M.I.; Bodnarchuk, M.J.; Grotevent, Kovalenko, M.V. Fast anion-exchange in highly luminescent nanocrystals of cesium lead halide perovskites (CsPbX_3 , X = Cl, Br, I). *Nano Lett.* **2015**, *15*, 5635–5640. [[CrossRef](#)]
60. Travis, W.; Glover, E.N.K.; Bronstein, H.; Scanlon, D.O.; Palgrave, R.G. On the application of the tolerance factor to inorganic and hybrid halide perovskites: A revised system. *Chem. Sci.* **2016**, *7*, 4548–4556. [[CrossRef](#)]
61. Manser, J.S.; Christians, J.A.; Kamat, P.V. Intriguing optoelectronic properties of metal halide perovskites. *Chem. Rev.* **2016**, *116*, 12956–13008. [[CrossRef](#)] [[PubMed](#)]
62. Worhatch, R.J.; Kim, H.; Swainson, I.P.; Yonkeu, A.L.; Billinge, S.J. Study of local structure in selected organic-inorganic perovskites in the $\text{Pm}\bar{3}\text{m}$ Phase. *Chem. Mater.* **2008**, *20*, 1272–1277. [[CrossRef](#)]
63. Baikie, T.; Fang, Y.; Kadro, J.M.; Schreyer, M.; Wei, F.; Mhaisalkar, S.G.; Graetzel, M.; White, T.J. Synthesis and crystal chemistry of the hybrid perovskite $(\text{CH}_3\text{NH}_3)\text{PbI}_3$ for solid-state sensitised solar cell applications. *J. Mater. Chem.* **2013**, *1*, 5628–5641. [[CrossRef](#)]
64. Weller, M.T.; Weber, O.J.; Henry, P.F.; Di Pumpo, A.M.; Hansen, T.C. Complete structure and cation orientation in the perovskite photovoltaic methylammonium lead iodide between 100 and 352 K. *Chem. Commun.* **2015**, *51*, 4180–4183. [[CrossRef](#)]
65. Brivio, F.; Walker, A.B.; Walsh, A. Structural and electronic properties of hybrid perovskites for high-efficiency thin-film photovoltaics from first-principles. *APL Mater.* **2013**, *1*, 042111. [[CrossRef](#)]
66. Eames, C.; Frost, J.M.; Barnes, P.R.; O'Regan, B.C.; Walsh, A.; Islam, M.S. Ionic transport in hybrid lead iodide perovskite solar cells. *Nat. Commun.* **2015**, *6*, 7497. [[CrossRef](#)]
67. Leppert, L.; Reyes-Lillo, S.E.; Neaton, J.B. Electric field-and strain-induced Rashba effect in hybrid halide perovskites. *J. Phys. Chem. Lett.* **2016**, *7*, 3683–3689. [[CrossRef](#)] [[PubMed](#)]

68. Amat, A.; Mosconi, E.; Ronca, E.; Quarti, C.; Umari, P.; Nazeeruddin, M.K.; Gratzel, M.; De Angelis, F. Cation-induced band-gap tuning in organohalide perovskites: Interplay of spin-orbit coupling and octahedra tilting. *Nano Lett.* **2014**, *14*, 3608–3616. [[CrossRef](#)] [[PubMed](#)]
69. Stamplecoskie, K.G.; Manser, J.S.; Kamat, P.V. Dual nature of the excited state in organic-inorganic lead halide perovskites. *Energy Environ. Sci.* **2015**, *8*, 208–215. [[CrossRef](#)]
70. Protesescu, S.; Yakunin, M.I.; Bodnarchuk, F.; Krieg, R.; Caputo, C.H.; Hendon, R.X.; Yang, A.; Walsh; Kovalenko, M.V. Nanocrystals of cesium lead halide perovskites (CsPbX₃, X = Cl, Br, and I): Novel optoelectronic materials showing bright emission with wide color gamut. *Nano Lett.* **2015**, *15*, 3692–3696. [[CrossRef](#)]
71. Jellicoe, T.C.; Richter, J.M.; Glass, H.F.J.; Tabachnyk, M.; Brady, R.; Dutton, S.E.; Rao, A.; Friend, R.H.; Credgington, D.; Greenham, N.C.; et al. Synthesis and optical properties of lead-free cesium tin halide perovskite nanocrystals. *J. Am. Chem. Soc.* **2016**, *138*, 2941–2944. [[CrossRef](#)]
72. Yin, W.J.; Shi, T.; Yan, Y. Superior photovoltaic properties of lead halide perovskites: Insights from first-principles theory. *J. Phys. Chem. C* **2015**, *119*, 5253–5264. [[CrossRef](#)]
73. Le, Q.V.; Hong, K.; Jang, H.W.; Kim, S.Y. Halide perovskite quantum dots for light-emitting diodes: Properties, synthesis, applications, and outlooks. *Adv. Electron. Mater.* **2018**, *4*, 1800335. [[CrossRef](#)]
74. Li, X.; Wu, Y.; Zhang, S.; Cai, B.; Gu, Y.; Song, J.; Zeng, H. CsPbX₃ Quantum dots for lighting and displays: Room-temperature synthesis, photoluminescence superiorities, underlying origins and white light-emitting diodes. *Adv. Funct. Mater.* **2016**, *26*, 2435–2445. [[CrossRef](#)]
75. Liang, J.; Zhao, P.; Wang, C.; Wang, Y.; Hu, Y.; Zhu, G.; Ma, L.; Liu, J.; Jin, Z. CsPb_{0.9}Sn_{0.1}IBr₂ based all-inorganic perovskite solar cells with exceptional efficiency and stability. *J. Am. Chem. Soc.* **2017**, *139*, 14009–14012. [[CrossRef](#)]
76. Luo, J.; Zhang, W.; Yang, H.; Fan, Q.; Xiong, F.; Liu, S.; Li, D.; Liu, B. Halide perovskite composites for photocatalysis: A mini review. *EcoMat* **2021**, *3*, 12079. [[CrossRef](#)]
77. Ng, C.H.; Ripolles, T.S.; Hamada, K.; Teo, S.H.; Lim, H.N.; Bisquert, J.; Hayase, S. Tunable open circuit voltage by engineering inorganic cesium lead bromide/iodide perovskite solar cells. *Sci. Rep.* **2018**, *8*, 2482. [[CrossRef](#)] [[PubMed](#)]
78. Guo, S.H.; Zhou, J.; Zhao, X.; Sun, C.Y.; You, S.Q.; Wang, X.L.; Su, Z.M. Enhanced CO₂ photoreduction via tuning halides in perovskites. *J. Catal.* **2019**, *369*, 201–208. [[CrossRef](#)]
79. Wang, T.; Daiber, B.; Frost, J.M.; Mann, S.A.; Garnett, E.C.; Walsh, A.; Ehrler, B. Indirect to direct bandgap transition in methylammonium lead halide perovskite. *Energy Environ. Sci.* **2017**, *10*, 509–515. [[CrossRef](#)]
80. Brenner, T.M.; Egger, D.A.; Kronik, L.; Hodes, G.; Cahen, D. Hybrid organic-inorganic perovskites: Low-cost semiconductors with intriguing charge-transport properties. *Nat. Rev. Mater.* **2016**, *1*, 15007. [[CrossRef](#)]
81. Sutherland, B.R.; Sargent, E.H. Perovskite photonic sources. *Nat. Photonics* **2016**, *10*, 295–302. [[CrossRef](#)]
82. Xing, J.; Yan, F.; Zhao, Y.; Chen, S.; Yu, H.; Zhang, Q.; Zeng, R.; Demir, H.V.; Sun, X.; Huan, A.; et al. High-efficiency light emitting diodes of organometal halide perovskite amorphous nanoparticles. *ACS Nano* **2016**, *10*, 6623–6630. [[CrossRef](#)] [[PubMed](#)]
83. Vargas, B.; Ramos, E.; Perez-Gutierrez, E.; Alonso, J.C.; Solis-Ibarra, D. A direct bandgap copper-antimony halide perovskite. *J. Am. Chem. Soc.* **2017**, *139*, 9116–9119. [[CrossRef](#)] [[PubMed](#)]
84. Meinardi, F.; Akkerman, Q.A.; Bruni, F.; Park, S.; Mauri, M.; Dang, Z.; Manna, L.; Brovelli, S. Doped halide perovskite nanocrystals for reabsorption-free luminescent solar concentrators. *ACS Energy Lett.* **2017**, *2*, 2368–2377. [[CrossRef](#)]
85. Pan, G.; Bai, X.; Yang, D.; Chen, X.; Jing, P.; Qu, S.; Zhang, L.; Zhou, D.; Zhu, J.; Xu, W.; et al. Doping lanthanide into perovskite nanocrystals: Highly improved and expanded optical properties. *Nano Lett.* **2017**, *17*, 8005–8011. [[CrossRef](#)]
86. Liu, M.; Zhong, G.; Yin, Y.; Miao, J.; Li, K.; Wang, C.; Xu, X.; Shen, C.; Meng, H. Aluminum-doped cesium lead bromide perovskite nanocrystals with stable blue photoluminescence used for display backlight. *Adv. Sci.* **2017**, *4*, 1700335. [[CrossRef](#)] [[PubMed](#)]
87. Stam, W.V.D.; Geuchies, J.J.; Altantzis, T.; Bos, K.H.W.V.D.; Meeldijk, J.D.; Aert, S.V.; Bals, S.; Vanmaekelbergh, D.; Donega, C.D.M. Highly emissive divalent-ion-doped colloidal CsPb_{1-x}M_xBr₃ perovskite nanocrystals through cation exchange. *J. Am. Chem. Soc.* **2017**, *139*, 4087–4097. [[CrossRef](#)]
88. Chen, J.; Dong, C.; Idriss, H.; Mohammed, O.F.; Bakr, O.M. Metal halide perovskites for solar-to-chemical fuel conversion. *Adv. Energy Mater.* **2020**, *10*, 1902433. [[CrossRef](#)]
89. Kudo, A.; Miseki, Y. Heterogeneous photocatalyst materials for water splitting. *Chem. Soc. Rev.* **2009**, *38*, 253–278. [[CrossRef](#)]
90. Navarro, R.M.; Alvarez-Galvan, M.C.; La Villoria de Mano, J.A.; Al-Zahrani, S.M.; Fierro, J.L.G. A framework for visible-light water splitting. *Energy Environ. Sci.* **2010**, *3*, 1865. [[CrossRef](#)]
91. Reza Gholipour, M.; Dinh, C.-T.; Beland, F.; Do, T.-O. Nanocomposite heterojunctions as sunlight-driven photocatalysts for hydrogen production from water splitting. *Nanoscale* **2015**, *7*, 8187–8208. [[CrossRef](#)] [[PubMed](#)]
92. Takanabe, K. Photocatalytic water splitting: Quantitative approaches toward photocatalyst by design. *ACS Catal.* **2017**, *7*, 8006–8022. [[CrossRef](#)]
93. Ponceca, C.S., Jr.; Savenije, T.J.; Abdellah, M.; Zheng, K.; Yartsev, A.; Pascher, T.; Harlang, T.; Chabera, P.; Pullerits, T.; Stepanov, A.; et al. Organometal halide perovskite solar cell materials rationalized: Ultrafast charge generation, high and microsecond-long balanced mobilities, and slow recombination. *J. Am. Chem. Soc.* **2014**, *136*, 5189–5192. [[CrossRef](#)] [[PubMed](#)]
94. Ball, J.M.; Petrozza, A. Defects in perovskite-halides and their effects in solar cells. *Nat. Energy* **2016**, *1*, 16149. [[CrossRef](#)]
95. Walsh, A.; Stranks, S.D. Taking control of ion transport in halide perovskite solar cells. *ACS Energy Lett.* **2018**, *3*, 1983–1990. [[CrossRef](#)]

96. De Wolf, S.; Holovsky, J.; Moon, S.J.; Loper, P.; Niesen, B.; Ledinsky, M.; Haug, F.J.; Yum, J.H.; Ballif, C. Organometallic halide perovskites: Sharp optical absorption edge and its relation to photovoltaic performance. *J. Phys. Chem. Lett.* **2014**, *5*, 1035–1039. [[CrossRef](#)]
97. Park, N.G. Perovskite solar cells: An emerging photovoltaic technology. *Mater. Today* **2015**, *18*, 65–72. [[CrossRef](#)]
98. Chen, K.; Deng, X.; Dodekatos, G.; Tüysüz, H. Photocatalytic polymerization of 3, 4-ethylenedioxythiophene over cesium lead iodide perovskite quantum dots. *J. Am. Chem. Soc.* **2017**, *139*, 12267–12273. [[CrossRef](#)]
99. Jiang, Q.; Zhao, Y.; Zhang, X.; Yang, X.; Chen, Y.; Chu, Z.; Ye, Q.; Li, X.; Yin, Z.; You, J. Surface passivation of perovskite film for efficient solar cells. *Nat. Photonics* **2019**, *13*, 460–466. [[CrossRef](#)]
100. Maes, J.; Balcaen, L.; Drijvers, E.; Zhao, Q.; De Roo, J.; Vantomme, A.; Vanhaecke, F.; Geiregat, P.; Hens, Z. Light absorption coefficient of CsPbBr₃ perovskite nanocrystals. *J. Phys. Chem. Lett.* **2018**, *9*, 3093–3097. [[CrossRef](#)]
101. Dong, Q.; Fang, Y.; Shao, Y.; Mulligan, P.; Qiu, J.; Cao, L.; Huang, J. Electron-hole diffusion lengths > 175 μm in solution-grown CH₃NH₃PbI₃ single crystals. *Science* **2015**, *347*, 967–970. [[CrossRef](#)] [[PubMed](#)]
102. Zhang, F.; Yang, B.; Li, Y.; Deng, W.; He, R. Extra long electron-hole diffusion lengths in CH₃NH₃PbI_{3-x}Cl_x perovskite single crystals. *J. Mater. Chem. C* **2017**, *5*, 8431–8435. [[CrossRef](#)]
103. Yettapu, G.R.; Talukdar, D.; Sarkar, S.; Swarnkar, A.; Nag, A.; Ghosh, P.; Mandal, P. Terahertz conductivity within colloidal CsPbBr₃ perovskite nanocrystals: Remarkably high carrier mobilities and large diffusion lengths. *Nano Lett.* **2016**, *16*, 4838–4848. [[CrossRef](#)] [[PubMed](#)]
104. Li, M.; Bhaumik, S.; Goh, T.W.; Kumar, M.S.; Yantara, N.; Gratzel, M.; Mhaisalkar, S.; Mathews, N.; Sum, T.C. Slow cooling and highly efficient extraction of hot carriers in colloidal perovskite nanocrystals. *Nat. Commun.* **2017**, *8*, 14350. [[CrossRef](#)]
105. Mondal, N.; Samanta, A. Complete ultrafast charge carrier dynamics in photo-excited all-inorganic perovskite nanocrystals (CsPbX₃). *Nanoscale* **2017**, *9*, 1878–1885. [[CrossRef](#)] [[PubMed](#)]
106. Wu, K.; Liang, G.; Shang, Q.; Ren, Y.; Kong, D.; Lian, T. Ultrafast interfacial electron and hole transfer from CsPbBr₃ perovskite quantum dots. *J. Am. Chem. Soc.* **2015**, *137*, 12792–12795. [[CrossRef](#)]
107. Wang, J.; Liu, J.; Du, Z.; Li, Z. Recent advances in metal halide perovskite photocatalysts: Properties, synthesis and applications. *J. Energy Chem.* **2021**, *54*, 770–785. [[CrossRef](#)]
108. Zhu, X.Y.; Podzorov, V. Charge carriers in hybrid organic-inorganic lead halide perovskites might be protected as large polarons. *J. Phys. Chem. Lett.* **2015**, *6*, 4758–4761. [[CrossRef](#)]
109. Sun, S.; Tominaka, S.; Lee, J.H.; Xie, F.; Cheetham, A.K. Synthesis, crystal structure, and properties of a perovskite-related bismuth phase, (NH₄)₃Bi₂I₉. *APL Mater.* **2016**, *4*, 031101. [[CrossRef](#)]
110. Wu, Y.; Wang, P.; Guan, Z.; Liu, J.; Wang, Z.; Zheng, Z.; Jin, S.; Dai, Y.; Whangbo, M.H.; Huang, B. Enhancing the photocatalytic hydrogen evolution activity of mixed halide perovskite CH₃NH₃PbBr_{3-x}I_x achieved by bandgap funneling of charge carriers. *ACS Catal.* **2018**, *8*, 10349–10357. [[CrossRef](#)]
111. Zhao, Z.; Wu, J.; Zheng, Y.Z.; Li, N.; Li, X.; Ye, Z.; Lu, S.; Tao, X.; Chen, C. Stable hybrid perovskite MAPb(I_{1-x}Br_x)₃ for photocatalytic hydrogen evolution. *Appl. Catal. B Environ.* **2019**, *253*, 41–48. [[CrossRef](#)]
112. Powers, D.C.; Hwang, S.J.; Zheng, S.L.; Nocera, D.G. How to apply metal halide perovskites to photocatalysis: Challenges and development. *Inorg. Chem.* **2014**, *53*, 9122–9128. [[CrossRef](#)] [[PubMed](#)]
113. Guan, Z.; Wu, Y.; Wang, P.; Zhang, Q.; Wang, Z.; Zheng, Z.; Liu, Y.; Dai, Y.; Whangbo, M.-H.; Huang, B. Perovskite photocatalyst CsPbBr_{3-x}I_x with a bandgap funnel structure for H₂ evolution under visible light. *Appl. Catal. B Environ.* **2019**, *245*, 522–527. [[CrossRef](#)]
114. Li, R.; Li, X.T.; Wu, J.J.; Lv, X.D.; Zheng, Y.Z.; Zhao, Z.J.; Ding, X.Q.; Tao, X.; Chen, J.F. Few-layer black phosphorus-on-MAPbI₃ for superb visible-light photocatalytic hydrogen evolution from HI splitting. *Appl. Catal. B Environ.* **2019**, *259*, 118075. [[CrossRef](#)]
115. Wang, H.; Wang, X.; Chen, R.; Zhang, H.; Wang, X.; Wang, J.; Zhang, J.; Mu, L.; Wu, K.; Fan, F.; et al. Promoting photocatalytic H₂ evolution on organic-inorganic hybrid perovskite nanocrystals by simultaneous dual-charge transportation modulation. *ACS Energy Lett.* **2019**, *4*, 40–47. [[CrossRef](#)]
116. Wang, F.; Liu, X.; Zhang, Z.; Min, S. A noble-metal-free MoS₂ nanosheet-coupled MAPbI₃ photocatalyst for efficient and stable visible-light-driven hydrogen evolution. *Chem. Comm.* **2020**, *56*, 3281–3284. [[CrossRef](#)]
117. Guo, Y.M.; Liu, G.N.; Li, Z.X.; Lou, Y.B.; Chen, J.X.; Zhao, Y.X. A stable lead-free (CH₃NH₃)₃Bi₂I₉ perovskite for photocatalytic hydrogen generation. *ACS Sustain. Chem. Eng.* **2019**, *7*, 15080–15085. [[CrossRef](#)]
118. Wang, T.; Yue, D.; Li, X.; Zhao, Y. Lead-free double perovskite Cs₂AgBiBr₆/RGO composite for efficient visible light photocatalytic H₂ evolution. *Appl. Catal. B Environ.* **2020**, *268*, 118399. [[CrossRef](#)]
119. Ju, D.X.; Zheng, X.P.; Liu, J.L.; Chen, Y.; Zhang, J.; Cao, B.Q.; Xiao, H.; Mohammed, O.F.; Bakr, O.M.; Tao, X.T. Reversible band gap narrowing of Sn-based hybrid perovskite single crystal with excellent phase stability. *Angew. Chem. Int. Ed.* **2018**, *57*, 14868–14872. [[CrossRef](#)]
120. Li, Z.J.; Hofman, E.; Li, J.; Davis, A.H.; Tung, C.-H.; Wu, L.Z.; Zheng, W.W. Photoelectrochemically active and environmentally stable CsPbBr₃/TiO₂ core/shell nanocrystals. *Adv. Funct. Mater.* **2018**, *28*, 1704288. [[CrossRef](#)]
121. Zhao, Z.; Wu, J.; Zheng, Y.Z.; Li, N.; Li, X.; Tao, X. Ni₃C-decorated MAPbI₃ as visible light photocatalyst for H₂ evolution from HI splitting. *ACS Catal.* **2019**, *9*, 8144–8152. [[CrossRef](#)]
122. Cai, C.; Teng, Y.; Wu, J.H.; Li, J.Y.; Chen, H.Y.; Chen, J.H.; Kuang, D.B. In situ photosynthesis of an MAPbI₃/CoP hybrid heterojunction for efficient photocatalytic hydrogen evolution. *Adv. Funct. Mater.* **2020**, *30*, 2001478. [[CrossRef](#)]

123. Zhao, H.; Chordiya, K.; Leukkunen, P.; Popov, A.; Upadhyay Kahaly, M.; Kordas, K.; Ojala, S. Dimethylammonium iodide stabilized bismuth halide perovskite photocatalyst for hydrogen evolution. *Nano Res.* **2021**, *14*, 1116–1125. [[CrossRef](#)]
124. Tang, Y.; Mak, C.H.; Liu, R.; Wang, Z.; Ji, L.; Song, H.; Tan, C.; Barriere, F.; Hsu, H.Y. In situ formation of bismuth-based perovskite heterostructures for high-performance cocatalyst-free photocatalytic hydrogen evolution. *Adv. Funct. Mater.* **2020**, *30*, 2006919. [[CrossRef](#)]
125. Liu, F.; Wang, M.; Liu, X.; Wang, B.; Li, C.; Liu, C.; Lin, Z.; Huang, F. A rapid and robust light-and-solution-triggered in situ crafting of organic passivating membrane over metal halide perovskites for markedly improved stability and photocatalysis. *Nano Lett.* **2021**, *21*, 1643–1650. [[CrossRef](#)] [[PubMed](#)]
126. Zhao, X.; Chen, S.; Yin, H.; Jiang, S.; Zhao, K.; Kang, J.; Liu, P.F.; Jiang, L.; Zhu, Z.; Cui, D.; et al. Perovskite microcrystals with intercalated monolayer MoS₂ nanosheets as advanced photocatalyst for solarpowered hydrogen generation. *Matter* **2020**, *3*, 935–949. [[CrossRef](#)]
127. Zhang, Y.; Shi, J.; Ding, X.; Wu, J.; Zheng, Y.Z.; Tao, X. Stable mixed-organic-cation perovskite MA_{1-x}FA_xPbI₃ integrated with MoS₂ for enhanced visible-light photocatalytic H₂ evolution. *Ind. Eng. Chem. Res.* **2020**, *59*, 20667–20675. [[CrossRef](#)]
128. Zhao, H.; Li, Y.; Zhang, B.; Xu, T.; Wang, C. Pt_x/[(CH₃)₂NH₂]₃[BiI₆] as a welldispersed photocatalyst for hydrogen production in hydroiodic acid. *Nano Energy* **2018**, *50*, 665–674. [[CrossRef](#)]
129. Teo, S.; Ng, C.; Ng, Y.; Islam, A.; Hayase, S.; Taufiq-Yap, Y. Resolve deep-rooted challenges of halide perovskite for sustainable energy development and environmental remediation. *Nano Energy* **2022**, *99*, 107401. [[CrossRef](#)]

Disclaimer/Publisher's Note: The statements, opinions and data contained in all publications are solely those of the individual author(s) and contributor(s) and not of MDPI and/or the editor(s). MDPI and/or the editor(s) disclaim responsibility for any injury to people or property resulting from any ideas, methods, instructions or products referred to in the content.